Probing PIEZO1 localization upon activation using high-resolution Atomic Force and Confocal Microscopy

Andra C. Dumitru[1#], Amaury Stommen[2#], Melanie Koehler[1], Anne-Sophie Cloos[2], Jinsung Yang[1], Arnaud Leclercqz[1], Donatienne Tyteca[2], David Alsteens[1]**

[1]Louvain Institute of Biomolecular Science and Technology, Université catholique de Louvain, Louvain-la-Neuve, Belgium.

[2] de Duve Institute, Université catholique de Louvain, Brussels, Belgium.

KEYWORDS: PIEZO1 clusters, Atomic force microscopy, single-molecule force spectroscopy, ion channel, red blood cells, laser scanning confocal microscopy, mechanotransduction

ABSTRACT

PIEZO1 ion channels are activated by mechanical stimuli, triggering intracellular chemical signals. Recent structural studies suggest that plasma membrane tension or local curvature changes modulate PIEZO1 channel gating and activation. However, whether PIEZO1 localization is governed by tension gradients or long-range mechanical perturbations across the cells is still unclear. Here, we probe the nanoscale localization of PIEZO1 on red blood cells (RBCs) at high-resolution (~30 nm) and we report for the first time the existence for submicrometric PIEZO1 clusters in native conditions. Upon interaction with Yoda1, an allosteric modulator, PIEZO1 clusters increase in abundance in regions of higher membrane tension and lower curvature. We further show that PIEZO1 ion channels interact with the spectrin cytoskeleton in both resting and activated states. Our results point towards a strong interplay between plasma membrane tension gradients, local curvature and cytoskeleton association of PIEZO1.

INTRODUCTION

PIEZO1 is a mechanosensitive ion channel associated with numerous physiological functions such as erythrocyte volume regulation, epithelial cell adhesion, blood vessel formation and development of vascular architecture[1-3]. Impaired PIEZO1 function has been linked to erythrocyte osmotic fragility and impairment of vascular development[4, 5]. Conversely, gain-of-function PIEZO1 mutations lead to decreased intracellular red blood cell (RBC) volume and hemolysis[6, 7]. Recently published cryo-electron microscopy structures of purified PIEZO1 provide detailed information of its homotrimeric structure consisting of three propeller blades extending away from a central cap region[8-11] (**Figure 1A**). Recent studies suggest that the blades and the helical beams attaching them to the cap region may efficiently transfer mechanical forces from lipids to the pore via a lever mechanism (**Figure 1A**)[12, 13]. So far, experiments on lipid bilayers[14], proteoliposomes[15], membrane patches[16] and bleb membranes[17] provided proof that PIEZO1 is sensitive to lateral membrane tension and can sense forces directly transmitted through the membrane. In this *force-from-lipids* model, the ion channel is gated by mechanical perturbations in the surrounding lipid bilayer[18, 19]. While the *force-from-lipid* paradigm has been firmly established for bacterial mechanosensitive channels (MscL and MscS) and eukaryotic TREK, TRAAK or two-pore domain K^+ (K_2P) channels [20, 21], it contrasts with the *force-from-filament tether model* in which mechanogating occurs via connections to the cytoskeleton or extracellular tethers[22-24]. Multiple studies used heterologous systems and showed that the cytoskeleton is not essential for PIEZO1 gating[17, 25, 26], but there is conflicting evidence that PIEZO1 can sense and respond to localized or long-range mechanical perturbations either exogenously applied or endogenously originated exists[27-29]. Furthermore, it also remains unclear why PIEZO1 is recruited to cell-junction or focal adhesion sites[30, 31] and whether it forms domains that could facilitate recruitment at appropriate plasma membrane location.

Here we use confocal imaging and force-distance based atomic force microscopy (FD-AFM) to determine the distribution of PIEZO1 prior and after activation by Yoda1, a high potency allosteric modulator[12, 15]. We first identify the presence of submicrometric PIEZO1 clusters in native conditions at the surface of RBCs, an ideal cell model to study PIEZO1 localization and activation as the RBC surface is featureless, with different curvature and tension areas, and RBCs constitutively expresses PIEZO1 allowing for Ca2+ entry. We further observe that PIEZO1

localization, accessibility and local density are regulated by membrane tension and local curvature. PIEZO1 cluster abundance is increased in areas of high membrane tension in response to Yoda1. FD-AFM and confocal imaging show that the lateral organization of PIEZO1 follows a spectrin mesh-like distribution. Taken together, PIEZO1 cluster regulation by membrane tension and cytoskeleton anchoring support the coexistence of *force-from-lipid* and *force-from-filament* gating models upon PIEZO1 ion channel activation.

RESULTS AND DISCUSSION

Probing PIEZO1 ion channels by FD-AFM

In order to evaluate the distribution of PIEZO1 on RBCs, we used a polyclonal PIEZO1-antibody, which demonstrated a high specificity towards PIEZO1 on RBC ghosts, as shown in Western blot experiments (**Figure S1A)**. We then validated the use of this antibody to specifically bind the extracellular domain of PIEZO1 ion channels on model surfaces and RBCs using force-volume (FV) and FD-AFM (**Figure 1B,C** and **Figure S2**). Thus, we covalently grafted single PIEZO1-antibodies to the free end of a heterobifunctional polyethylene glycol (PEG) linker attached to the AFM tip. In a first approach, to mimic cell-surface PIEZO1 ion channels *in vitro*, a fragment of PIEZO1 was covalently immobilized on gold surfaces using carbodiimide crosslinker chemistry (**Figure 1B**). PIEZO1-antibody AFM tips were used to probe the binding properties of the complex formed with PIEZO1 ion channels fragments grafted on model surfaces by FV-AFM (see **Methods** and **Figure S2A-C**). Specific adhesion events were observed in ~6% of the retraction FD curves at rupture distances > 10 nm, corresponding to the extension of the PEG linker-antibody complex (**Figure 1D** curves 1, 2). FD curves displaying no adhesion events or unspecific adhesion events were discarded from further analysis (**Figure 1D** curves 3, 4). For specific binding interactions, rupture forces of 71 ± 21 pN (mean ± standard deviation (S.D.); N=588 data points) at 1 µm s^{-1} retraction speed were detected (**Figure 1E**). To further validate the specificity, two independent control experiments were performed: (*i*) a competition assay by injecting 1 µM free PIEZO1-antibody in the solution and (*ii*) a negative control using AFM tips functionalized with a non-specific IgG isotype similar in size to PIEZO1-antibody (**Figure S1B,C)**. We observed a significantly lower binding frequency, below 2% *versus* 6% compared to our standard condition (PIEZO1-antibody tips probing recombinant PIEZO1 fragments-functionalized surfaces). In agreement with above data, the average rupture force is 69 ± 20

pN in our standard conditions and similar values of 66 ± 24 pN are obtained following an injection of PIEZO1-antibodies (Welch's T-test: p=0.101, ns). Rupture forces quantified for anti-gH/gL tips probed on the same surface coated with recombinant PIEZO1 fragments are of 42 ± 13pN, which is 30% lower than in normal conditions and statistically relevant (Welch's T-test: p=2.88E-15), confirming the specificity of the set-up to detect PIEZO1 fragments (**Figure S1C**).

Similarly, we probed RBCs that naturally express PIEZO1 ion channels and have the great advantage of displaying featureless surfaces, making them a good model for membrane studies. To preserve the cellular biconcavity, RBCs were instantaneously fixed in suspension, and then immobilized on poly-L-lysine (PLL) coated glass petri dishes and imaged with the PIEZO1-antibody functionalized tips (**Figure 1C**) using FD-based AFM[32] (**Figure S2D**). Height and adhesion maps were simultaneously (see **Methods** and **Figure S2E,F**) and force *vs* time (FT) curves were analyzed in order to extract the rupture forces of specific adhesion events for each pixel in the images (**Figure S2A**). Around 2% of the FD curves showed specific adhesion events between PIEZO1-antibody and PIEZO1 ion channels (**Figure 1F** curves 1, 2), with rupture forces of 115 ± 26 pN (mean ± S.D, *N*=268 data points) at ~125 µm s^{-1} retraction speed (**Figure 1G**). Other FD curves showing either no adhesion or unspecific adhesion events were discarded for further quantification (**Figure 1F** curves 3, 4).

PIEZO1-antibody binding free-energy landscape

The rupture forces probed on model surfaces and on RBCs strongly differ due to the different tip velocities applied during the experiments. To unambiguously demonstrate that these rupture forces originated from the same binding partners, we characterized the kinetic parameters underlying the interaction between PIEZO1 and PIEZO1-antibody. In AFM-based single-molecule force spectroscopy studies, the application of an external force to a ligand-receptor bond adds a mechanical potential that tilts the free-energy landscape and lowers the free-energy barrier towards dissociation, thereby increasing the likelihood of unbinding by reducing the lifetime of the bond (**Figure 1H**)[33]. The Bell-Evans (BE) model predicts that the most probable rupture force in the thermally activated regime scales linearly with the logarithm of the loading rate (LR)[34].

We extracted the rupture forces and LRs from FT curves recorded on both model surfaces and RBCs (**Figure S3**) and we overlaid them in a dynamic force spectroscopy plot (**Figure 1I**, see

Methods). The extracted rupture forces show a linear dependency with the LR, spanning a broad range between 10^2 pN s^{-1} to 10^7 pN s^{-1}. We observed a very good alignment between the data obtained on purified ion channel fragments and RBCs, confirming the physiological relevance of our results obtained on model surfaces. The BE model was used to fit the data (Figure 1I, black lineI), assuming a simple two-state model where the bound and the unbound state are separated by a single energy barrier. From the slope of the fit, we estimated the length scale of the energy barrier x_u= 0.46 ± 0.04 nm and the kinetic off-rate (k_{off}) or dissociation rate is obtained from the intercept of the fit (at LR=0) yielding k_{off} values of 0.62 ± 0.41 s^{-1}. In addition, we also observed bivalent interactions that appear as uncorrelated bonds loaded in parallel, where the load is equally distributed among the existing bonds in an attachment, as predicted by the Williams-Evans (WE) model (Figure 1I, dashed line II)[35]. While grafted at low density, these double interactions could result from the fact that PIEZO1-antibodies have two antigen-binding sites.

PIEZO1 increased accessibility upon activation by Yoda1

The small molecule Yoda1 has been shown to activate PIEZO1 ion channels, acting as a gating modifier that potentiates its mechanosensitivity[12, 36]. The exact mechanism underlying this interaction is unknown, but PIEZO1 is thought to harbour a specific binding site for Yoda1 in the region between the anchor domain and the piezo repeat A98[3, 36] (Figure 2A). Recent studies evidenced that Yoda1 causes the ion channel to open up, which enables exchange of cations including calcium (Ca^{2+})[37] (Figure 2A). We therefore treated RBCs with Yoda1 at different concentrations to modulate PIEZO1 channel activity and followed Ca^{2+} accumulation using spectrofluorimetry and flow cytometry. In the 30-150 nM range, we observed a linear increase of intracellular Ca^{2+} content as a function of Yoda1 concentration (Figure 2B,C) and excluded any effect related to RBC hemolysis (Figure 2D). Higher Yoda1 concentrations induce a stronger Ca^{2+} intracellular accumulation (Figure S4K), but in RBCs this is accompanied by a loss of transversal membrane asymmetry (Figure S4L), required for PIEZO1 activation[38]. Moreover, a careful examination of RBC morphology showed that even at 100 nM, loss of RBC biconcavity is clearly visible in fixed RBCs (Figure S4A-J). We therefore decided to work at 50 nM Yoda1 for subsequent experiments.

We first studied the nanoscale distribution of PIEZO1 on RBCs in both resting and activated state using confocal laser scanning microscopy (CLSM, Figure 2E, F) and FD-AFM (Figure 2I-L).

Using CLSM, we started by checking the specificity of the PIEZO1-antibody (**Figure S5A**) and optimized the immunostaining procedure by instantaneous fixation in suspension using a mix of glutaraldehyde/paraformaldehyde to preserve the RBC biconcavity (see **Methods**) and by permeabilization with a Triton X-100 concentration that does not affect PIEZO1 organization at the RBC surface **(Figure S5B)**. We observed that PIEZO1 is distributed into clusters of ∼275 nm in diameter (**Figure 2E,F**). Yoda1 treatment leads to a significant 1.7-fold increase of the mean fluorescence intensity per RBC (**Figure 2G)** and a significantly higher number of PIEZO1 clusters compared to the control condition (**Figure 2H**). Previous electrophysiology experiments suggested that PIEZO1 could exist in discrete physical domains whose global properties can modify channel gating[39] and a very recent STORM superresolution imaging study using a PIEZO1-GFP fusion protein indicates that plasma membrane cholesterol domains coordinate the activity of clustered PIEZO1 channels[40]. However, to the best of our knowledge, this is the first report of PIEZO1 clustering in submicrometric domains observed in a native system.

AFM high-resolution height images and corresponding adhesion maps recorded with PIEZO1-antibody derivatized tips provide further insights into the localization of PIEZO1 at the RBC surface (**Figure 2I-L**). Notably, Yoda1 treatment of RBCs results in a significant 2-fold increase of the binding frequency from 1.8 ± 0.3 % to 3.5 ± 0.4 % (**Figure 2M**). However, the rise in binding frequency is not accompanied by a change of the mean rupture binding force, which remains constant in both control and Yoda1 conditions ($F_{\mathrm{control}} \sim 157 \pm 36$ pN, $F_{\mathrm{Yoda1}} \sim 159 \pm 21$ pN, **Figure 2N**). Together, these results support the fact that Yoda1 treatment induces an increase of the PIEZO1 accessibility.

Plasma membrane distribution of PIEZO1 clusters upon activation by Yoda1

While some previous studies have shown that PIEZO1 channels diffuse easily within the plasma membrane and are widely distributed throughout the cell[28], PIEZO1 activation is stress and stimuli dependent[40-42]. To further investigate this process, RBCs appear as a tool of choice thanks to their well-defined shape with various curvature and tension areas. It has been demonstrated that membrane forces are non-uniform along RBC membrane and that the force density and membrane tension are larger in the center/dimple than in the edge/rim[43]. Moreover, the presence of nanometer-scale heterogeneities[32] could indeed serve as reservoir for the generation of positive or negative curvature at the local level, which could induce channel gating. Therefore, we anticipated that PIEZO1 conformation and cluster localization

could be controlled by local membrane curvature and tension. To evaluate this hypothesis, we analyzed by CLSM and FD-AFM the PIEZO1 localization at the RBC edges *versus* the center before and after activation by Yoda1 (**Figure 3**). For CLSM experiments, RBCs were immunolabeled with PIEZO1-antibody enabling to quantify the PIEZO1 distribution in top and side view. The rim were associated to high curvature (HC) areas, while the dimple corresponded to low curvature (LC) regions (**Figure 3A**). Representative CLSM images of single RBCs before and after Yoda1 treatment are shown in **Figure 3B,C**.

We observed that Yoda1 modulation of PIEZO1 ion channels induces a significant increase of fluorescence intensity (**Figure 3D**) and abundance of PIEZO1 clusters in LC, but not in HC areas (**Figure 3E,F**). PIEZO1 is distributed into clusters of ~315 nm diameter in HC, compared with 260 nm in LC regions. Yoda1 treatment does not affect cluster size, which remains stable at ~275 nm diameter in HC *versus* 265 nm in LC regions (**Figure S6A,B**).

We used an analogous approach to quantify FD-AFM results. Specifically, based on the RBC round shape, we analyzed the distribution of PIEZO1 ion channels and classified their location into three concentric regions (*inner*, *median* and *outer*; **Figure 3A** and **Methods**). Adhesion maps of control and Yoda1-treated RBCs were analyzed and we extracted profile plots of normalized integrated intensities around *inner*, *median* and outer *regions* (**Figure 3G-L**). Before Yoda1 treatment, PIEZO1 are predominantly localized at the RBC *outer* rim, which is in line with the higher number of PIEZO1 clusters observed in the HC areas by CLSM (see **Figure 3F** *versus* **E**). After treatment by Yoda1, the presence of PIEZO1 in the *inner* and *median* regions is markedly increased, compared to a very slight increase in the *outer* region (**Figure 3M**).

The increased abundance of PIEZO1 in the dimple (LC or *inner* region) confirmed by AFM and CLSM suggests that, as an allosteric modulator, Yoda1 could induce conformational changes of the ion channel that increase the affinity towards the PIEZO1-antibody and the intrinsic curvature of PIEZO1 upon activation favors a stronger interaction with LC areas. Moreover, we hypothesize that the open pore conformation of PIEZO1 stabilized by Yoda1 treatment leads to more clusters of sufficient size to be resolved by confocal microscopy due to higher PIEZO1 membrane lateral diffusion. According to this hypothesis, PIEZO1-GFP shows a restricted lateral diffusion in the HEK293T plasma membrane while depletion of cholesterol, which is known to control membrane tension, causes a faster channel membrane diffusion[40].

The increased number of PIEZO1 clusters upon Yoda1 treatment correlates with previous findings pointing towards a higher force density and membrane tension in the dimple region of RBCs [43]. Our data are in good agreement with recent computational studies showing that myosin-mediated forces are not homogenously distributed along the RBC plasma membrane and that the force density is higher in the central region compared to the rim. These *in sillico* studies also speculated that PIEZO1 channels could localize preferentially in the dimple regions of RBCs as a result of surface tractions and the control exerted by membrane curvature [42]. This in agreement with the *force-from-lipids* model, which assumes that the channels respond to changes in membrane tension directly.

Deciphering PIEZO1-spectrin skeleton interplay

Cryo-electron tomography studies revealed that the RBC cytoskeleton is a densely packed heterogeneous network of filaments[44]. This two-dimensional cytoskeletal network has a quasi-hexagonal symmetry and consists of $(\alpha_1\beta_2)_2$ spectrin tetramers interconnected at short junctional complexes (JC) made of actin filaments, protein 4.1, tropomodulin and other associated proteins[44, 45] (Figure 4A). The RBC cytoskeleton is tethered to cell membrane by integral proteins such as Band3 or Glycophorin C (GPC) (Figure 4A). Band3 is actually the most abundant protein in the RBCs plasma membrane and half of Band3 proteins in RBCs associate either with ankyrin or protein 4.1, forming either ankyrin or JC[46]. Spectrin tetramers are found in a compressed state in the cytoskeletal network, and it is still a challenge to experimentally determine the actual ultrastructure of the erythrocyte cytoskeleton. Average lengths of spectrin tetramers estimated by different techniques range between 35-200 nm, while JC are just a fraction of around 30-50 nm[44, 47-50].

Besides the force-from-lipid model, the *force-from-filament* gating model suggests that mechanosensitive ion channels couple to extracellular structures or intracellular tethers (the cytoskeleton), which transmit macroscopic forces that induce mechanogating[24]. To evaluate if PIEZO1 channels might indeed use a complementary *force-from-filament* gating model to enable long-distance sensing of mechanical perturbation across an intact cell via the cytoskeleton, we tried to determine whether the location of PIEZO1 on RBCs could be governed by the underlying cytoskeleton.

We used CLSM to analyze the extent of PIEZO1 colocalization with spectrin and Band3, as main components involved in RBC mechanical homeostasis (Figure 4B-I). In control RBCs, the extent

of colocalization of PIEZO1 with spectrin is of ~0.45 and with Band3 of ~0.40 (**Figure 4J**, **Figure S7A**). Importantly, spectrin or PIEZO1 each decorated by one primary antibody recognized by two different secondary antibodies did not reach a coefficient higher than ~0.6 (**Figure S7B**). Moreover, and quite excitingly, Band3-spectrin colocalization coefficients are similar as for PIEZO1-spectrin and PIEZO1-Band3 (**Figure S7B**). The extent of PIEZO1 colocalization with spectrin or Band3 is not significantly different in Yoda1 treated RBCs (**Figure 4J; S7A**). Our hypothesis is that PIEZO1 ion channels interact with spectrin, which would enable them to be anchored in the RBC LC areas, where force density and tension are larger[43]. This would allow PIEZO1 to sense and respond to mechanical stimuli transduced as forces through the cytoskeleton[51]. To gain further insights about the PIEZO1-spectrin interaction hypothesis, we further analyzed multiparametric FD-AFM maps of control and Yoda1 treated RBCs (**Figure 4K,L** shows an example of control RBCs maps), focusing on the spatial distribution of PIEZO1 channels probed in AFM experiments. **Figure 4M** depicts a hexagonal lattice model, where each unit cell is made of 6 spectrin-like rods of 200 nm, overlaid with a representative region of an adhesion map (boxed region in **Figure 4L**). An overlay of the hexagonal lattice model with the localization of PIEZO1 (white dots correspond to adhesion events) evidences a very good correlation between lattice connection regions and PIEZO1 localization. Adhesive pixels localized at a distance <20 nm, representing the size of the PEG-PIEZO1-antibody complex tethered to the AFM tip apex, were marked with a red dot (**Figure 4M**). Our analysis shows that among the total number of PIEZO1 ion channels detected in our FD-AFM experiments, around 50% overlap with connection regions within the hexagonal lattice representing the cytoskeletal network.

We further examined unbinding events in adhesion maps of control and Yoda1 treated RBCs in terms of nearest neighbor distributions (see **Methods**). Histograms of nearest neighbor distances (**Figure 4N,O)** depict a multimodal distribution with peaks centered at 69 ± 7 nm, 119 ± 17 nm, 178 ± 47 nm and 254 ± 38 nm for control RBCs. Similar distances between probed PIEZO1 are found on Yoda1 treated RBCs, at 70 ± 16 nm, 123 ± 18 nm, 175 ± 46 nm and 255 ± 34 nm. Remarkably, our measured distances match well recent 3D-STORM experiments, where the calculated edge lengths for the cytoskeletal meshwork in RBCs is of ∼80 nm[50]. Given the distances between the probed ion channels, we confirm that PIEZO1 follow a meshwork distribution similar to the spectrin skeleton. Altogether, our data could suggest that PIEZO1 is tethered to spectrin-Band3 complexes.

For the first time, we spatially solved the distribution of PIEZO1 with high lateral resolution in native RBCs plasma membrane. We observe an increased abundance of PIEZO1 clusters in areas of higher membrane tension upon Yoda1 activation. High-resolution FD-AFM, supported by colocalization experiments using CLSM, evidences a cytoskeleton-like organization of PIEZO1, adopting a pattern similar to the spectrin mesh, and colocalizing with Band3 integral proteins. These results indicate that local membrane curvature and tension are key actors regulating PIEZO1 cluster localization, dynamics and accessibility, while cytoskeleton anchoring could have a role in reducing diffusion and stabilizing cluster formation. Together, the interplay between PIEZO1 localization, membrane tension and cytoskeleton organization support the coexistence of the force-from-lipid and the force-from-filament gating models, even if the mechanism behind the role of the cytoskeleton remains to be demonstrated. Our study opens new avenues for the understanding of PIEZO1-mediated mechanotransduction processes in living cells.

AUTHOR INFORMATION

Corresponding Authors

*E-mail: donatienne.tyteca@uclouvain.be and david.alsteens@uclouvain.be

Author Contributions

The manuscript was written through contributions of all authors. All authors have given approval to the final version of the manuscript. #these authors contributed equally.

Funding sources

This work was supported by the Université catholique de Louvain, the Fonds National de la Recherche Scientifique (F.R.S-FNRS; grant number: PDR T.0070.16 to D.A.) and the Research Department of the Communauté française de Belgique (Concerted Research Action). D.A and D.T. are Research Associate of the F.R.S.-FNRS. A.C.D and M.K are postdoctoral fellows of the F.R.S-FNRS.

Notes

The authors declare no competing financial interest.

ASSOCIATED CONTENT

Supporting Information. This material is available free of charge via the internet at https://pubs.acs.org. The Supporting Information file provides additional details on the experimental methods, data analysis and Figures S1-S6.

ACKNOWLEDGMENT

We thank Dr. Martin Delguste (Université catholique de Louvain, Belgium) for providing anti-gH/gL antibodies. Cartoons in Figures 1A-C, 2A, 3A, 4A and ToC graphic were created in Adobe Illustrator with support of BioRender.com.

REFERENCES

1. Cahalan, S. M.; Lukacs, V.; Ranade, S. S.; Chien, S.; Bandell, M.; Patapoutian, A., Piezo1 links mechanical forces to red blood cell volume. *eLife* **2015,** *4*, e07370.
2. Li, J.; Hou, B.; Tumova, S.; Muraki, K.; Bruns, A.; Ludlow, M. J.; Sedo, A.; Hyman, A. J.; McKeown, L.; Young, R. S.; Yuldasheva, N. Y.; Majeed, Y.; Wilson, L. A.; Rode, B.; Bailey, M. A.; Kim, H. R.; Fu, Z.; Carter, D. A. L.; Bilton, J.; Imrie, H.; Ajuh, P.; Dear, T. N.; Cubbon, R. M.; Kearney, M. T.; Prasad, K. R.; Evans, P. C.; Ainscough, J. F. X.; Beech, D. J., Piezo1 integration of vascular architecture with physiological force. *Nature* **2014,** *515* (7526), 279-282.
3. Kefauver, J. M.; Ward, A. B.; Patapoutian, A., Discoveries in structure and physiology of mechanically activated ion channels. *Nature* **2020,** *587* (7835), 567-576.
4. Lukacs, V.; Mathur, J.; Mao, R.; Bayrak-Toydemir, P.; Procter, M.; Cahalan, S. M.; Kim, H. J.; Bandell, M.; Longo, N.; Day, R. W.; Stevenson, D. A.; Patapoutian, A.; Krock, B. L., Impaired PIEZO1 function in patients with a novel autosomal recessive congenital lymphatic dysplasia. *Nat. Commun.* **2015,** *6* (1), 8329.
5. Zarychanski, R.; Schulz, V. P.; Houston, B. L.; Maksimova, Y.; Houston, D. S.; Smith, B.; Rinehart, J.; Gallagher, P. G., Mutations in the mechanotransduction protein PIEZO1 are associated with hereditary xerocytosis. *Blood* **2012,** *120* (9), 1908-1915.
6. Ma, S.; Cahalan, S.; LaMonte, G.; Grubaugh, N. D.; Zeng, W.; Murthy, S. E.; Paytas, E.; Gamini, R.; Lukacs, V.; Whitwam, T.; Loud, M.; Lohia, R.; Berry, L.; Khan, S. M.; Janse, C. J.; Bandell, M.; Schmedt, C.; Wengelnik, K.; Su, A. I.; Honore, E.; Winzeler, E. A.; Andersen, K. G.; Patapoutian, A., Common *PIEZO1* allele in African populations causes RBC dehydration and attenuates *Plasmodium* infection. *Cell* **2018,** *173* (2), 443-455.e12.
7. Albuisson, J.; Murthy, S. E.; Bandell, M.; Coste, B.; Louis-dit-Picard, H.; Mathur, J.; Fénéant-Thibault, M.; Tertian, G.; de Jaureguiberry, J.-P.; Syfuss, P.-Y.; Cahalan, S.; Garçon, L.; Toutain, F.; Simon Rohrlich, P.; Delaunay, J.; Picard, V.; Jeunemaitre, X.; Patapoutian, A., Dehydrated hereditary stomatocytosis linked to gain-of-function mutations in mechanically activated PIEZO1 ion channels. *Nat. Commun.* **2013,** *4* (1), 1884.
8. Saotome, K.; Murthy, S. E.; Kefauver, J. M.; Whitwam, T.; Patapoutian, A.; Ward, A. B., Structure of the mechanically activated ion channel Piezo1. *Nature* **2018,** *554* (7693), 481-486.
9. Zhao, Q.; Zhou, H.; Chi, S.; Wang, Y.; Wang, J.; Geng, J.; Wu, K.; Liu, W.; Zhang, T.; Dong, M.-Q.; Wang, J.; Li, X.; Xiao, B., Structure and mechanogating mechanism of the Piezo1 channel. *Nature* **2018,** *554* (7693), 487-492.
10. Ge, J.; Li, W.; Zhao, Q.; Li, N.; Chen, M.; Zhi, P.; Li, R.; Gao, N.; Xiao, B.; Yang, M., Architecture of the mammalian mechanosensitive Piezo1 channel. *Nature* **2015,** *527* (7576), 64-69.
11. Guo, Y. R.; MacKinnon, R., Structure-based membrane dome mechanism for Piezo mechanosensitivity. *eLife* **2017,** *6*, e33660.
12. Botello-Smith, W. M.; Jiang, W.; Zhang, H.; Ozkan, A. D.; Lin, Y.-C.; Pham, C. N.; Lacroix, J. J.; Luo, Y., A mechanism for the activation of the mechanosensitive Piezo1 channel by the small molecule Yoda1. *Nat. Commun.* **2019,** *10* (1), 4503.
13. Wang, Y.; Chi, S.; Guo, H.; Li, G.; Wang, L.; Zhao, Q.; Rao, Y.; Zu, L.; He, W.; Xiao, B., A lever-like transduction pathway for long-distance chemical- and mechano-gating of the mechanosensitive Piezo1 channel. *Nat. Commun.* **2018,** *9* (1), 1300.
14. Coste, B.; Xiao, B.; Santos, J. S.; Syeda, R.; Grandl, J.; Spencer, K. S.; Kim, S. E.; Schmidt, M.; Mathur, J.; Dubin, A. E.; Montal, M.; Patapoutian, A., Piezo proteins are pore-forming subunits of mechanically activated channels. *Nature* **2012,** *483* (7388), 176-181.

15. Syeda, R.; Xu, J.; Dubin, A. E.; Coste, B.; Mathur, J.; Huynh, T.; Matzen, J.; Lao, J.; Tully, D. C.; Engels, I. H.; Petrassi, H. M.; Schumacher, A. M.; Montal, M.; Bandell, M.; Patapoutian, A., Chemical activation of the mechanotransduction channel Piezo1. *eLife* **2015,** *4*, e07369.
16. Lewis, A. H.; Grandl, J., Mechanical sensitivity of Piezo1 ion channels can be tuned by cellular membrane tension. *eLife* **2015,** *4*, e12088.
17. Cox, C. D.; Bae, C.; Ziegler, L.; Hartley, S.; Nikolova-Krstevski, V.; Rohde, P. R.; Ng, C.-A.; Sachs, F.; Gottlieb, P. A.; Martinac, B., Removal of the mechanoprotective influence of the cytoskeleton reveals PIEZO1 is gated by bilayer tension. *Nature Communications* **2016,** *7* (1), 10366.
18. Kung, C., A possible unifying principle for mechanosensation. *Nature* **2005,** *436* (7051), 647-654.
19. Teng, J.; Loukin, S.; Anishkin, A.; Kung, C., The force-from-lipid (FFL) principle of mechanosensitivity, at large and in elements. *Pflügers Arch. Eur. J. Physiol.* **2015,** *467* (1), 27-37.
20. Martinac, B., The ion channels to cytoskeleton connection as potential mechanism of mechanosensitivity. *Biochim. Biophys. Acta* **2014,** *1838* (2), 682-691.
21. Cox, C. D.; Bavi, N.; Martinac, B., Chapter Three - Origin of the Force: The Force-From-Lipids Principle Applied to Piezo Channels. In *Curr. Top. Membr.*, Gottlieb, P. A., Ed. Academic Press: 2017; Vol. 79, pp 59-96.
22. Gillespie, P. G.; Walker, R. G., Molecular basis of mechanosensory transduction. *Nature* **2001,** *413* (6852), 194-202.
23. Markin, V. S.; Hudspeth, A. J., Gating-Spring Models of Mechanoelectrical Transduction by Hair Cells of the Internal Ear. *Annu. Rev. Biophys. Biomol. Struct.* **1995,** *24* (1), 59-83.
24. Nourse, J. L.; Pathak, M. M., How cells channel their stress: Interplay between Piezo1 and the cytoskeleton. *Semin. Cell Dev. Biol.* **2017,** *71*, 3-12.
25. Bavi, N.; Richardson, J.; Heu, C.; Martinac, B.; Poole, K., PIEZO1-Mediated Currents Are Modulated by Substrate Mechanics. *ACS Nano* **2019,** *13* (11), 13545-13559.
26. Romero, L. O.; Caires, R.; Nickolls, A. R.; Chesler, A. T.; Cordero-Morales, J. F.; Vásquez, V., A dietary fatty acid counteracts neuronal mechanical sensitization. *Nat. Commun.* **2020,** *11* (1), 2997.
27. Coste, B.; Mathur, J.; Schmidt, M.; Earley, T. J.; Ranade, S.; Petrus, M. J.; Dubin, A. E.; Patapoutian, A., Piezo1 and Piezo2 Are Essential Components of Distinct Mechanically Activated Cation Channels. *Science* **2010,** *330* (6000), 55-60.
28. Ellefsen, K. L.; Holt, J. R.; Chang, A. C.; Nourse, J. L.; Arulmoli, J.; Mekhdjian, A. H.; Abuwarda, H.; Tombola, F.; Flanagan, L. A.; Dunn, A. R.; Parker, I.; Pathak, M. M., Myosin-II mediated traction forces evoke localized Piezo1-dependent Ca^{2+} flickers. *Commun. Biol.* **2019,** *2* (1), 298.
29. Pathak, M. M.; Nourse, J. L.; Tran, T.; Hwe, J.; Arulmoli, J.; Le, D. T. T.; Bernardis, E.; Flanagan, L. A.; Tombola, F., Stretch-activated ion channel Piezo1 directs lineage choice in human neural stem cells. *Proc. Natl. Acad. Sci. U. S. A.* **2014,** *111* (45), 16148-16153.
30. Gudipaty, S. A.; Lindblom, J.; Loftus, P. D.; Redd, M. J.; Edes, K.; Davey, C. F.; Krishnegowda, V.; Rosenblatt, J., Mechanical stretch triggers rapid epithelial cell division through Piezo1. *Nature* **2017,** *543* (7643), 118-121.
31. Yao, M.; Tijore, A.; Cox, C. D.; Hariharan, A.; Van Nhieu, G. T.; Martinac, B.; Sheetz, M., Force-dependent Piezo1 recruitment to focal adhesions regulates adhesion maturation and turnover specifically in non-transformed cells. *bioRxiv* **2020**, 2020.03.09.972307.
32. Dumitru, A. C.; Poncin, M. A.; Conrard, L.; Dufrêne, Y. F.; Tyteca, D.; Alsteens, D., Nanoscale membrane architecture of healthy and pathological red blood cells. *Nanoscale Horiz.* **2018,** *3* (3), 293-304.
33. Evans, E.; Ritchie, K., Dynamic strength of molecular adhesion bonds. *Biophys. J.* **1997,** *72* (4), 1541-1555.
34. Müller, D. J.; Dumitru, A. C.; Lo Giudice, C.; Gaub, H. E.; Hinterdorfer, P.; Hummer, G.; De Yoreo, J. J.; Dufrêne, Y. F.; Alsteens, D., Atomic Force Microscopy-Based Force Spectroscopy and Multiparametric Imaging of Biomolecular and Cellular Systems. *Chem. Rev.* **2020** *Article ASAP*.
35. Williams, P. M., Analytical descriptions of dynamic force spectroscopy: behaviour of multiple connections. *Anal. Chim. Acta* **2003,** *479* (1), 107-115.

36. Lacroix, J. J.; Botello-Smith, W. M.; Luo, Y., Probing the gating mechanism of the mechanosensitive channel Piezo1 with the small molecule Yoda1. *Nat. Commun.* **2018,** *9* (1), 2029.
37. Xiao, B., Levering Mechanically Activated Piezo Channels for Potential Pharmacological Intervention. *Annu. Rev. Pharmacol. Toxicol.* **2020,** *60* (1), 195-218.
38. Tsuchiya, M.; Hara, Y.; Okuda, M.; Itoh, K.; Nishioka, R.; Shiomi, A.; Nagao, K.; Mori, M.; Mori, Y.; Ikenouchi, J.; Suzuki, R.; Tanaka, M.; Ohwada, T.; Aoki, J.; Kanagawa, M.; Toda, T.; Nagata, Y.; Matsuda, R.; Takayama, Y.; Tominaga, M.; Umeda, M., Cell surface flip-flop of phosphatidylserine is critical for PIEZO1-mediated myotube formation. *Nat. Commun.* **2018,** *9* (1), 2049.
39. Bae, C.; Gnanasambandam, R.; Nicolai, C.; Sachs, F.; Gottlieb, P. A., Xerocytosis is caused by mutations that alter the kinetics of the mechanosensitive channel PIEZO1. *Proc Natl Acad Sci U S A* **2013,** *110* (12), E1162-E1168.
40. Ridone, P.; Pandzic, E.; Vassalli, M.; Cox, C. D.; Macmillan, A.; Gottlieb, P. A.; Martinac, B., Disruption of membrane cholesterol organization impairs the activity of PIEZO1 channel clusters. *J. Gen. Physiol.* **2020,** *152* (8): e201912515.
41. Cox, C. D.; Gottlieb, P. A., Amphipathic molecules modulate PIEZO1 activity. *Biochem. Soc. Trans.* **2019,** *47* (6), 1833-1842.
42. Svetina, S.; Švelc Kebe, T.; Božič, B., A Model of Piezo1-Based Regulation of Red Blood Cell Volume. *Biophys. J.* **2019,** *116* (1), 151-164.
43. Alimohamadi, H.; Smith, A. S.; Nowak, R. B.; Fowler, V. M.; Rangamani, P., Non-uniform distribution of myosin-mediated forces governs red blood cell membrane curvature through tension modulation. *PLOS Comput. Biol.* **2020,** *16* (5), e1007890.
44. Nans, A.; Mohandas, N.; Stokes, David L., Native Ultrastructure of the Red Cell Cytoskeleton by Cryo-Electron Tomography. *Biophys. J.* **2011,** *101* (10), 2341-2350.
45. Fowler, V. M., Chapter Two - The Human Erythrocyte Plasma Membrane: A Rosetta Stone for Decoding Membrane–Cytoskeleton Structure. In *Curr. Top. Membr.*, Bennett, V., Ed. Academic Press: 2013; Vol. 72, pp 39-88.
46. Alenghat, F. J.; Golan, D. E., Chapter Three - Membrane Protein Dynamics and Functional Implications in Mammalian Cells. In *Curr. Top. Membr.*, Bennett, V., Ed. Academic Press: 2013; Vol. 72, pp 89-120.
47. Byers, T. J.; Branton, D., Visualization of the protein associations in the erythrocyte membrane skeleton. *Proc. Natl. Acad. Sci. U. S. A.* **1985,** *82* (18), 6153-6157.
48. Liu, S. C.; Derick, L. H.; Palek, J., Visualization of the hexagonal lattice in the erythrocyte membrane skeleton. *J. Cell. Biol.* **1987,** *104* (3), 527-536.
49. Lux, S. E., IV, Anatomy of the red cell membrane skeleton: unanswered questions. *Blood* **2016,** *127* (2), 187-199.
50. Pan, L.; Yan, R.; Li, W.; Xu, K., Super-Resolution Microscopy Reveals the Native Ultrastructure of the Erythrocyte Cytoskeleton. *Cell Rep.* **2018,** *22* (5), 1151-1158.
51. Wang, J.; Jiang, J.; Yang, X.; Wang, L.; Xiao, B., Tethering Piezo channels to the actin cytoskeleton for mechanogating via the E-cadherin-β-catenin mechanotransduction complex. *bioRxiv* **2020**, 2020.05.12.092148.

FIGURES

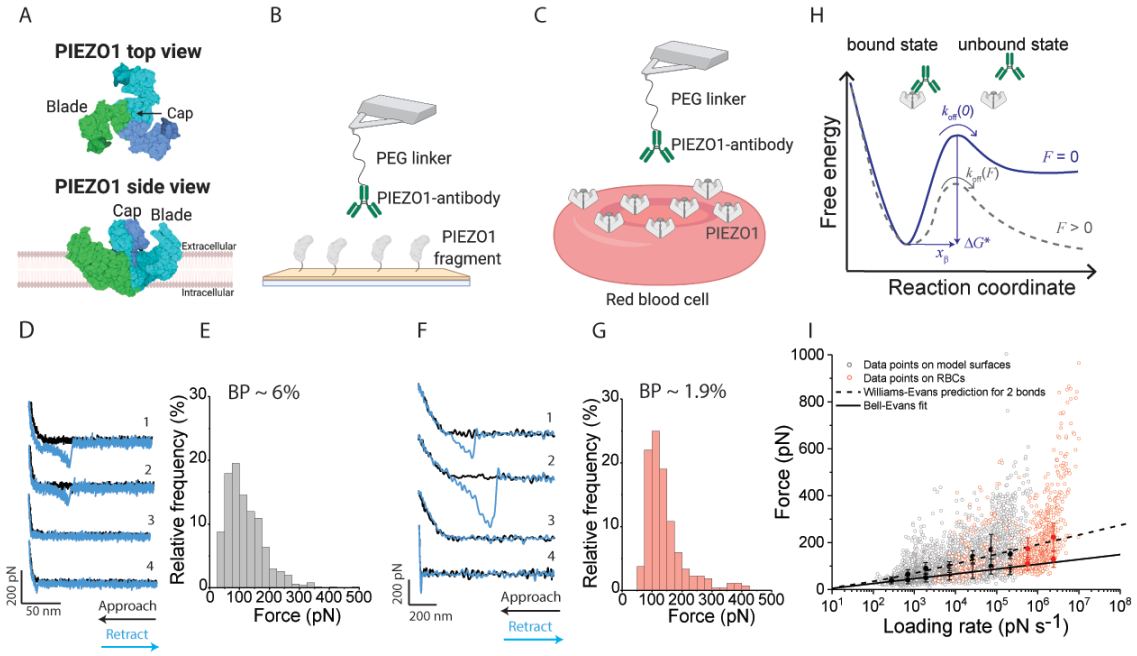

Figure 1. Probing PIEZO1 binding using a PIEZO1-antibody functionalized AFM tip. (A) Cartoon representation of PIEZO1 side and top views, where each subunit is colored differently (PDB: 6B3R). PIEZO1 is a homotrimer protein with three propeller blades extending away from the central cap region. (B) Interactions between recombinant PIEZO1 protein fragment and the PIEZO1-antibody are monitored by AFM on model surfaces, where a PIEZO1 fragment is covalently coupled to a gold surface with NHS/EDC chemistry. (C) AFM tips functionalized with PIEZO1-antibody were used to probe PIEZO1 ion channels on RBCs naturally expressing the protein. (D) Examples of FD curves recorded on model surfaces coated with recombinant PIEZO1 protein fragments and (E) the corresponding unbinding forces histogram at 1 µm s^{-1}. (F) FD curves obtained while probing PIEZO1 receptors on the surface of RBCs and (G) the corresponding unbinding forces histogram at 125 µm s^{-1}. (H) Free energy landscape of PIEZO1-PIEZO1-antibody complexes unbinding. A single potential barrier separates the bound and the unbound states of a two-state unbinding process (blue line). The activation free energy of unbinding is ΔG^* and x_β represents the transition between the bound and the unbound states along the reaction coordinate. In equilibrium conditions (F=0), the energy barrier is spontaneously crossed at a transition rate $k_{off}(0)$. The application of an external force to the bond (F>0) tilts the energy landscape (dotted grey line), lowering the energy barrier. Probing the interaction forces of a (bio)molecular bond over a wide range of loading rates allows determination of the parameters describing the free-energy barrier stabilizing the bond, such as x_β and the off-rate k_{off}. (I) Dynamic force spectroscopy plot showing the dependence of the rupture force on the loading rate when probing the interaction between PIEZO1-antibody and either model surfaces coated with recombinant PIEZO1 protein fragments (empty black dots, N=3006) or PIEZO1 ion channels on the surface of RBCs (empty red dots N=816). The most probable rupture forces calculated from the Gaussian fits in Figure S3 are represented as filled black and red dots, mean ± S.D. The solid line represents the fit of the data using the Bell-Evans model and the dotted line is the Williams-Evans prediction for two parallel bonds. In panels E,G, BP represents the binding probability and bin width is 25 pN. The data is representative of at least 5 independent experiments. Panels A-C created with BioRender.com.

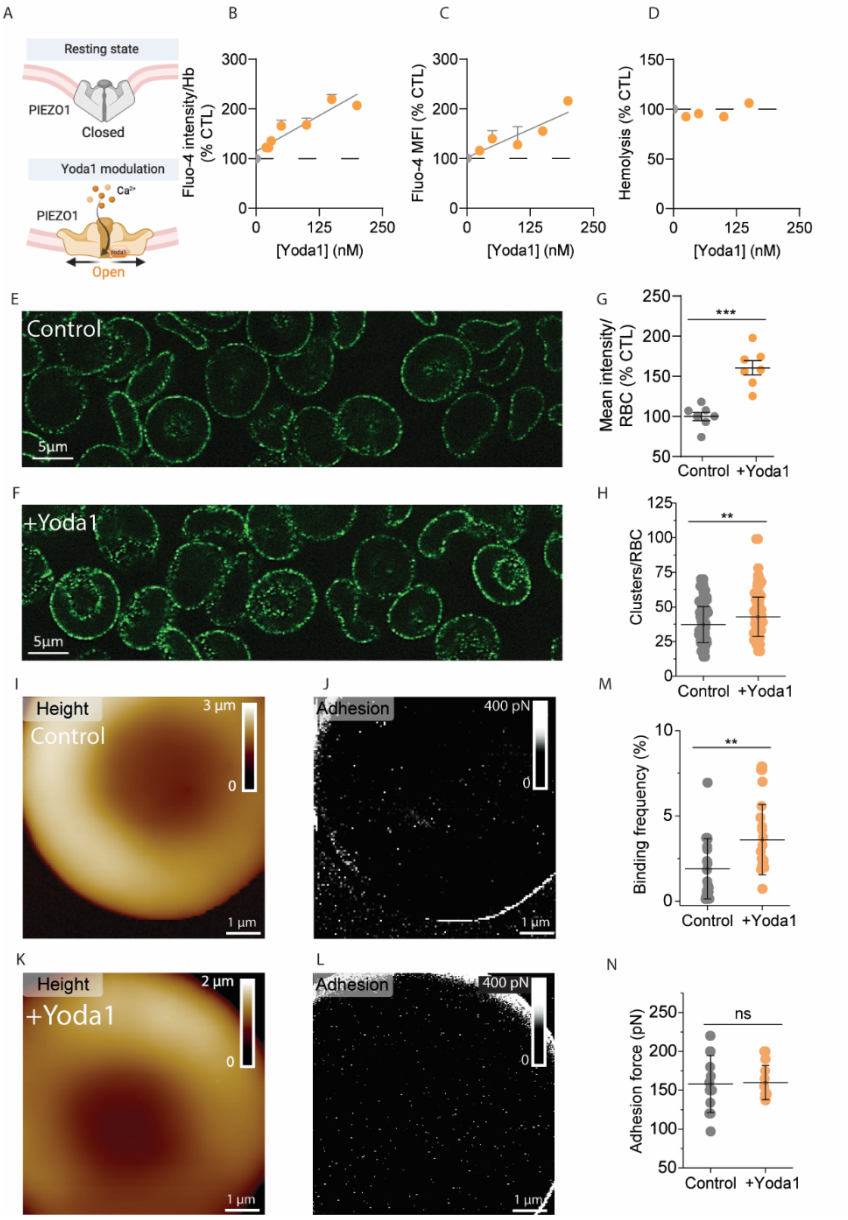

Figure 2. Probing resting state and chemically activated PIEZO1 on the surface of RBCs. (A) In resting state, the PIEZO1 pore has a closed conformation. Yoda1 stabilizes the open conformation of the PIEZO1 channel, allowing for ion exchange. The three propeller blades are thought to induce a local curvature around the central pore of PIEZO1 and could be used as levers to sense tension-induce flattening of the plasma membrane and open the pore. (B,C) Intracellular calcium content of Yoda1 treated RBCs was assessed by fluorimetry (B) or by flow cytometry (C). Fluorimetry data were normalized to hemoglobin (Hb) content and median fluorescence intensity (MFI) was determined from flow cytometry data. (D) Extent of RBC hemolysis upon treatment with Yoda1. (E,F) PIEZO1 distribution observed on fixed and permeabilized RBCs by confocal microscopy in control (E) and Yoda1 treated conditions. (G) Quantification of mean fluorescence intensity per immunolabeled RBC. (H) Quantification of PIEZO1 clusters abundance per immunolabeled RBC. (I,K) FD-based AFM topography images and (J,L) corresponding adhesion of control and RBCs treated with Yoda1. (M) Binding frequencies measured when probing a PIEZO1-antibody functionalized AFM tip against control (grey) or Yoda1 treated cells (yellow). (N) Adhesion forces measured on control (grey) and Yoda1 treated cells (yellow). Results in (B,C,D,G) are expressed as percentage of the control condition. Results are presented as means ± SEM of 3-12 experiments in B, means ± SD of 2 experiments in C, and means of 3 experiments in D. Each dot represents one independent experiment in G. Each dot represents a single RBC from at least 3 independent experiments in H,M,N. %CTL is defined as percent control. ns: not significant **: p< 0.01 and ***: p< 0.001. Panel A was created with BioRender.com.

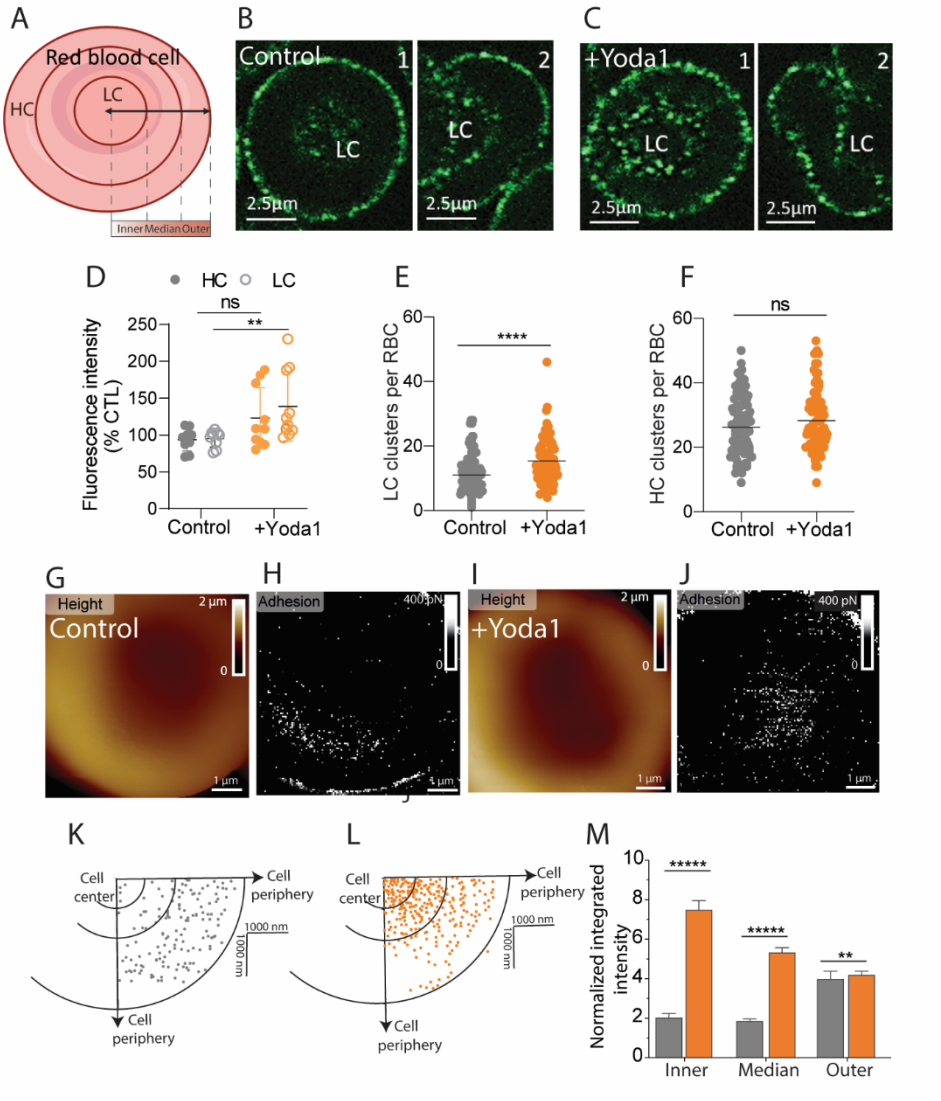

Figure 3. Quantification of PIEZO1 receptors clustering on the surface of RBCs. (A) Schematic representation of a RBC displaying a low curvature (LC) area in the central region and a high curvature (HC) area on the rim. The 2D horizontal projection of the RBC surface was divided by three concentric circles, representing the inner, median and outer areas. (B,C) Representative CSLM images of single RBCs showing PIEZO1 distribution in LC areas for control and Yoda1-treated RBCs. 1, RBC in upper view; 2, RBC in side view. (D) Quantification of fluorescence intensity in HC (filled circles) and LC (empty circles) areas of CTL (grey) and Yoda1-treated (orange) RBCs. (E,F) Abundance of PIEZO1 clusters in (E) LC and in (F) HC areas for control and Yoda1-treated RBCs. (G-J) FD-based AFM height images and corresponding adhesion maps of (G,H) control and (I,J) Yoda1-treated RBCs. (K,L) Spatial distribution of specific PIEZO1 unbinding events in the adhesion maps (H) and (L), as a function of the distance from the center of the cell. (M) Adhesion maps were used to calculate normalized integrated intensity of PIEZO1-antibody adhesion events in the inner, median or outer regions of control (grey) and Yoda1-treated (orange) RBCs. Bar range represents data mean ± SEM of 3-10 representative experiments. Ns: not significant; **: $p<0.01$; ****: $p<0.0001$ and *****: $p<0.00001$. Yoda1-treated RBCs represent cells treated with 50 nM Yoda1. Panel A created with BioRender.com.

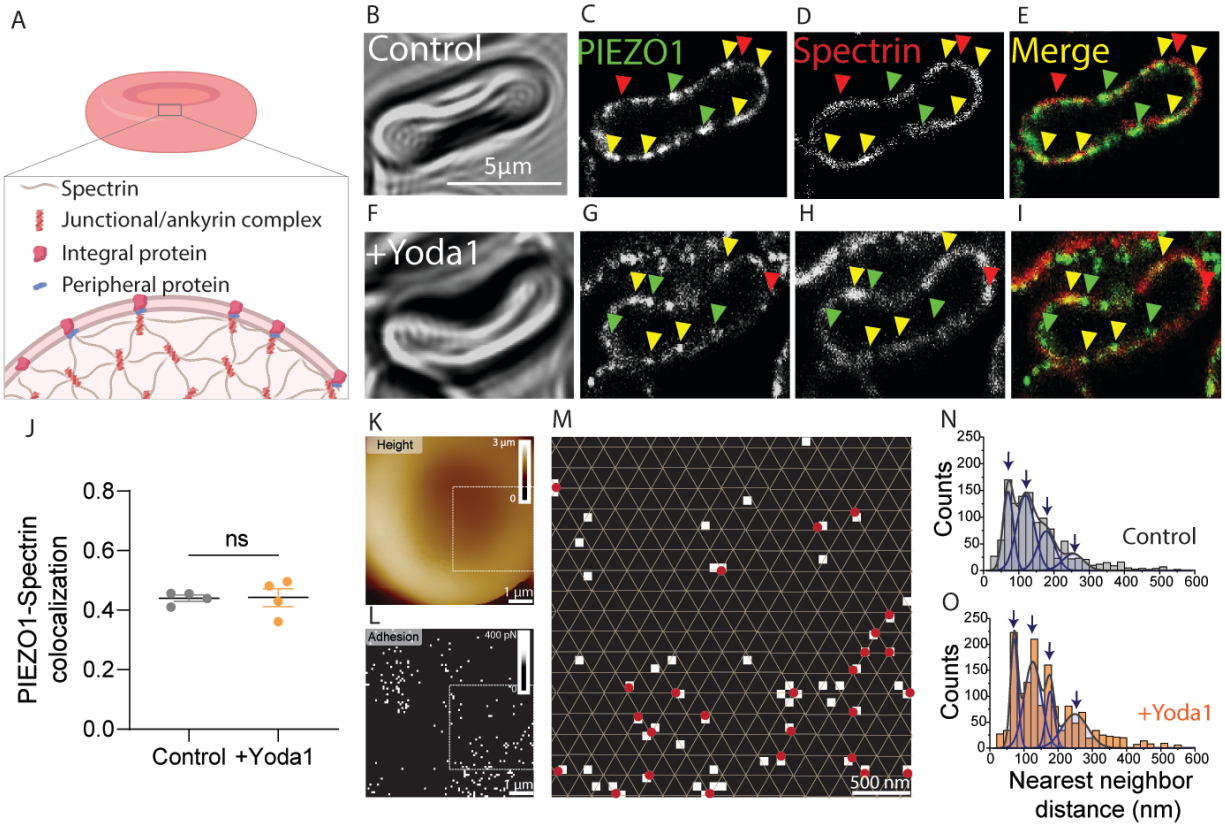

Figure 4. PIEZO1 association with the spectrin skeleton. (A) Schematic representation of the RBC cytoskeleton. The two-dimensional cytoskeletal meshwork has a quasi-hexagonal symmetry and has as main components $(\alpha_1\beta_2)_2$ spectrin tetramers connected by junctional/ankyrin complexes. The RBC cytoskeleton is tethered to the plasma membrane through peripheral and integral proteins. (B-I) Representative confocal images of PIEZO1-spectrin colocalization in control and Yoda1-treated RBCs after fixation with 4% PAF and 0.05% Glut and permeabilization with 1% Triton X-100 for 15 min. Green and red arrowheads correspond to PIEZO1 or spectrin only; yellow arrowheads, colabeling. Lefts panels are provided to highlight the preservation of the RBC morphology. (J) Quantification of the extent of colocalization between PIEZO1 and spectrin from the confocal images shown in B-I. (K,L) Representative FD-AFM height and adhesion maps of a single RBC probed with a PIEZO1-antibody AFM tip. (M) Overlay of a hexagonal lattice model and the boxed region in the adhesion map in (L). Each unit cell in the hexagonal network consists of 6 spectrin-like rods 200 nm in length. Red dots evidence overlap of PIEZO1 adhesion events and lattice connection points. (N,O) Histograms of nearest neighbor distribution for adhesion events extracted from representative control and Yoda1 treated adhesion maps. A multimodal distribution of the distances is observed for both conditions. Bin width is 20 nm, blue lines represent individual Gaussian fits and dark grey lines global Gaussian fits. Results are from at least 4 independent experiments. Ns: not significant. Panel A was created with BioRender.com.

531 ToC graphic

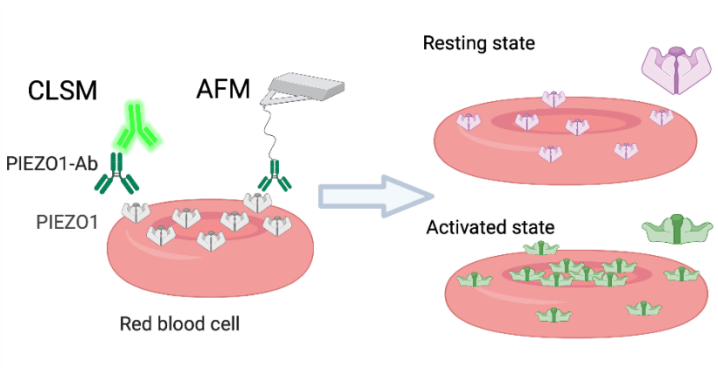

532